Sphingomyelin distribution in lipid rafts of artificial monolayer membranes visualized by Raman microscopy

Jun Ando[a,b,c,d], Masanao Kinoshita[e,f,1], Jin Cui[e,g], Hiroyuki Yamakoshi[a,d], Kosuke Dodo[a,b,d], Katsumasa Fujita[a,b,c], Michio Murata[e,g,2], and Mikiko Sodeoka[a,b,d,2]

[a]Sodeoka Live Cell Chemistry Project, Japan Science and Technology Agency (JST), Exploratory Research for Advanced Technology, Saitama 351-0198, Japan; [b]Core Research for Evolutionary Science and Technology (CREST), JST, Saitama 351-0198, Japan; [c]Department of Applied Physics, Osaka University, Osaka 565-0871, Japan; [d]Synthetic Organic Chemistry Laboratory, RIKEN, Saitama 351-0198, Japan; and [e]Lipid Active Structure Project, JST, Exploratory Research for Advanced Technology, [f]Project Research Center for Fundamental Science, and [g]Department of Chemistry, Graduate School of Science, Osaka University, Osaka 560-0043, Japan

Edited by Michael L. Klein, Temple University, Philadelphia, PA, and approved March 10, 2015 (received for review September 19, 2014)

Sphingomyelin (SM) and cholesterol (chol)-rich domains in cell membranes, called lipid rafts, are thought to have important biological functions related to membrane signaling and protein trafficking. To visualize the distribution of SM in lipid rafts by means of Raman microscopy, we designed and synthesized an SM analog tagged with a Raman-active diyne moiety (diyne-SM). Diyne-SM showed a strong peak in a Raman silent region that is free of interference from intrinsic vibrational modes of lipids and did not appear to alter the properties of SM-containing monolayers. Therefore, we used Raman microscopy to directly visualize the distribution of diyne-SM in raft-mimicking domains formed in SM/dioleoylphosphatidylcholine/chol ternary monolayers. Raman images visualized a heterogeneous distribution of diyne-SM, which showed marked variation, even within a single ordered domain. Specifically, diyne-SM was enriched in the central area of raft domains compared with the peripheral area. These results seem incompatible with the generally accepted raft model, in which the raft and nonraft phases show a clear biphasic separation. One of the possible reasons is that gradual changes of SM concentration occur between SM-rich and -poor regions to minimize hydrophobic mismatch. We believe that our technique of hyperspectral Raman imaging of a single lipid monolayer opens the door to quantitative analysis of lipid membranes by providing both chemical information and spatial distribution with high (diffraction-limited) spatial resolution.

lipid raft | Raman imaging | alkyne tag | supported monolayer | sphingomyelin

Specific membrane microdomains, called lipid rafts, are thought to have important biological functions in cells (1, 2). The rafts are frequently defined as detergent-resistant membrane domains and enriched in sphingomyelin (SM) and cholesterol (chol). Certain membrane proteins, such as glycosylphosphatidylinositol-anchored proteins and acylated cytosolic proteins, are considered to show preferential association with those raft lipids, which thereby, facilitate various biological functions, including membrane trafficking and signal transduction (3). Therefore, an understanding of the distribution of SMs within lipid rafts is expected to provide basic information about site-specific cellular functions.

The basic features of lipid rafts have often been examined using SM/phosphatidylcholine (PC)/chol mixtures as model membrane systems, because these ternary mixtures undergo phase separation into raft-like ordered domains and fluid disordered domains (4). In addition, the membrane properties of these ordered domains, such as detergent insolubility, are similar to those of lipid rafts in biomembranes (5). However, there are few reports on the lipid distribution in the raft mixtures, because detergent extraction provokes reorganization of the lipids and consequently, obscures information about the inherent domains (6). Thus, direct observation is essential to investigate the lipid distribution in intact lipid preparations.

Fluorescence microscopy has been widely used to observe phase separation in lipid membranes (7), and fluorescently labeled lipids or lipophilic dyes have generally been used as imaging agents (8). However, these fluorescent lipids are frequently excluded from the raft-like ordered domains, probably because the large fluorophores perturb the lipid packing (8, 9). So far, there is no lipid probe that can directly visualize the distribution of intrinsic SM molecules in multicomponent membranes, although some peptide-based large probes that recognize raft domains have been developed (10, 11). Consequently, direct observation of SM distribution in lipid rafts has not proved feasible with fluorescence-based imaging modalities.

Here, we focused on spontaneous Raman scattering microscopy to directly and chemoselectively visualize the distribution of a lipid constituent in lipid rafts using a ternary lipid monolayer system as a model. Raman spectroscopy has chemical specificity, because it detects characteristic molecular vibration frequencies. The molecular distribution in a sample can be determined by Raman microscopy, and the image has quantitative chemical contrast, because the scattering intensity is proportional to the number of molecules in the detection volume. A molecule-specific full spectrum is obtained for each pixel, allowing us to analyze the

Significance

Phase separation in lipid rafts has been observed with fluorescently labeled lipids, but they are often excluded from the ordered domain because of the steric effect of the bulky fluorophore on lipid packing, making it difficult to analyze the interior of the raft domain. Here, we synthesized an analog of sphingomyelin tagged with a small Raman active diyne moiety, which provides high chemical selectivity without affecting the membrane properties. Raman microscopy successfully visualized, at single lipid-layer sensitivity, a heterogeneous spatial distribution of this probe within raft-like ordered domains, which was different from the generally accepted raft model. This approach provides both chemical selectivity and quantitative imaging capability and is useful for functional studies of lipid rafts.

Author contributions: J.A., M.K., K.D., M.M., and M.S. designed research; J.A., M.K., J.C., and H.Y. performed research; K.F. contributed new reagents/analytic tools; J.A., M.K., and K.F. analyzed data; and J.A., M.K., K.F., M.M., and M.S. wrote the paper.

The authors declare no conflict of interest.

This article is a PNAS Direct Submission.

[1]Present address: Department of Chemistry, Faculty of Science, Kyushu University, Fukuoka 812-8581, Japan.

[2]To whom correspondence may be addressed. Email: murata@chem.sci.osaka-u.ac.jp or sodeoka@riken.jp.

This article contains supporting information online at www.pnas.org/lookup/suppl/doi:10.1073/pnas.1418088112/-/DCSupplemental.

molecular composition and state of the lipid mixture at each position, with the help of accumulated knowledge on Raman spectra of lipid membranes obtained over the last few decades (12). Because Raman microscopy uses an optical detection scheme, minimally invasive noncontact observation of a sample can be achieved under atmospheric pressure.

Despite these advantages, spontaneous Raman microscopy has not yet been used for imaging of lipid rafts to our knowledge. It is partly because Raman imaging of a single lipid membrane has long been thought to be infeasible from a sensitivity point of view owing to the extremely weak scattering signal from the limited number of lipid molecules in the detection volume (13). Spatial resolution is also restricted by the imaging time, because a weak scattering signal tends to require a long exposure time, resulting in limited pixel numbers for imaging within a realistic observation time. However, recent developments in spontaneous Raman microscopy have allowed us to overcome this problem; efficient optical systems and a parallel Raman excitation/detection configuration (14–16) improve imaging speed with both high sensitivity and high diffraction-limited spatial resolution.

As a target lipid component for observation by Raman microscopy in a raft-containing membrane, we focused on SM, and newly synthesized an SM analog with a Raman-active alkyne moiety. Alkyne is a promising tag in terms of both its small chemical structure and its high Raman scattering intensity in the silent region of biomolecules, allowing selective detection of alkyne-tagged molecules (17, 18). We first attempted Raman imaging using a propargyl-SM analog with a single alkyne group, but the intensity was insufficient for imaging. Because a conjugated diyne group shows a stronger Raman band (18), we next aimed to introduce a 6-hydroxy-hexa-2,4-diynyl group at the ammonium moiety of the head group; the 6-hydroxyl group was expected to increase the hydrophilicity of this relatively hydrophobic Raman tag (Fig. 1). We found that diyne-SM was effective for spontaneous Raman imaging of SM in a raft-mimicking ternary monolayer system.

Results

The Raman spectra in Fig. 2 are those of supported monolayer membranes consisting of SM (Fig. 2*A*), diyne-SM (Fig. 2*B*), dioleoyl-PC (DOPC) (Fig. 2*C*), and chol (Fig. 2*D*). As shown in Fig. 2*B*, the diyne-SM monolayer showed a strong peak at 2,263 cm^{-1}, which is attributed to the stretching vibrational mode of the diyne moiety (18). Because the peak appears in the silent region of membrane lipids, it would be possible to unambiguously identify diyne-SM in multicomponent membranes by means of Raman spectroscopy without any interference from intrinsic vibrational modes of other membrane constituents. For this measurement, 532-nm laser light was focused onto the membrane by using an objective lens to excite Raman scattering from the lipid. It was

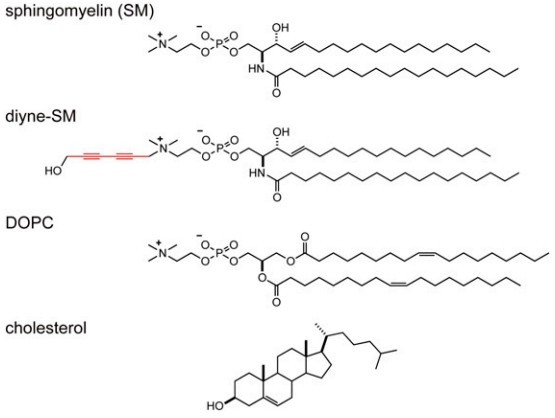

Fig. 1. Chemical structures of SM, diyne-SM, DOPC, and chol.

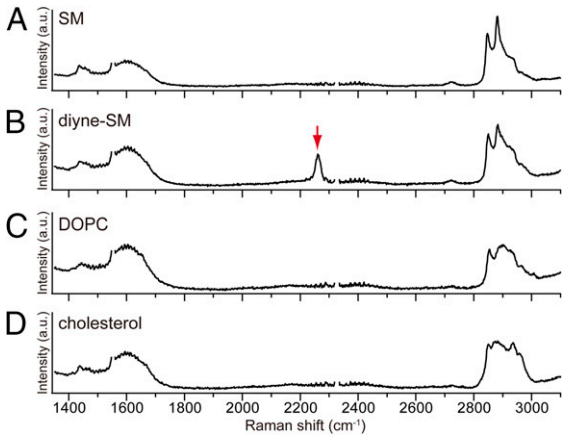

Fig. 2. Raman spectra of supported lipid monolayers of (*A*) SM, (*B*) diyne-SM, (*C*) DOPC, and (*D*) chol on a quartz substrate. The Raman peak of diyne at 2,263 cm^{-1} is marked by a red arrow. The supported sample was prepared at 12 mN/m and 25 °C using the LB technique. Raman measurement was performed 15 times at different positions in each membrane, with an exposure time of 6 s. Averaged Raman spectra are shown. Raman peaks of O_2 at ∼1,555 cm^{-1} and N_2 at ∼2,330 cm^{-1} have been deleted so that Raman peaks from lipid molecules can be clearly seen, which is explained in Fig. S1.

confirmed that our microscope was able to acquire a Raman spectrum from a small, diffraction-limited area within a lipid monolayer, with a signal-to-noise ratio sufficient to detect the Raman peak of the diyne moiety.

Next, we observed a diyne-SM/DOPC/chol ternary monolayer (1:1:1 molar ratio) by laser Raman microscopy in a point-scanning mode. SM-based lipid monolayer and bilayer are known to have similar phase segregation properties (4, 19); moreover, by using a monolayer, we can exclude possible asymmetry of lipid composition between the two layers that would weaken the contrast of Raman images. The Raman image, reconstructed from the peak intensity of diyne at 2,264 cm^{-1}, visualized a heterogeneous distribution of diyne-SM (Fig. 3*A*), which was concentrated in micrometer-sized round domains. When an image was constructed using the peak bottom intensity at 2,222 cm^{-1}, it showed no contrast or distribution, ruling out the possibility that artifacts affected the imaging (Fig. 3*B*). We also performed Raman imaging of lipid membrane (Fig. 4 *A*–*C*) with three different composition ratios of diyne-SM/DOPC/chol (molar ratios of 1:1:1, 3:7:3, and 1:0:0). Phase segregation occurred at the 1:1:1 ratio, whereas uniform distributions were observed for 3:7:3 and 1:0:0 ratios. The difference between Fig. 4 *A* and *B* can be accounted for by the notion that the increased content of chol leads to recruitment of SM from the disordered phase and increases the concentration of SM in the ordered domains (20). Judging from the image contrast, the density of diyne-SM is higher in ordered domains at a 1:1:1 ratio (Fig. 4*A*) than at a 3:7:3 ratio (Fig. 4*B*) but lower than that at a 1:0:0 ratio (Fig. 4*C*). The averaged diyne peak intensity of the ordered domains in Fig. 4*A* was ∼2.3 times higher than that of the disordered region in Fig. 4*A* when the domains were separated based on the mean value of the entire Raman image (Fig. S2 and Table S1). On the same basis, the diyne-SM density in the ordered domains in Fig. 4*A* was 52.2% of the diyne-SM density in Fig. 4*C* (Fig. S2 and Table S1). Note that spatial variations of the signal in Fig. 4*C* (Fig. S2*E*) are mainly caused by the low signal-to-noise ratio in the detection as summarized in Table S1.

Hyperspectral Raman imaging, as performed in this experiment, allows us to examine spatially resolved Raman spectra at different phases in the diyne-SM/DOPC/chol ternary monolayer (Fig. 4 *D* and *E* and Fig. S3). In particular, the intensity profile of lipid CH_2/CH_3 stretching at 2,800–3,000 cm^{-1} was different between the raft-like ordered domains and the disordered domain (Fig. 4*D*). The peak profile of CH_2/CH_3 stretching (such as sharp peaks at 2,850 and 2,883 cm^{-1}) in the raft-like ordered domains was

CHEMISTRY

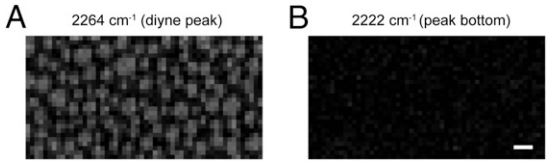

Fig. 3. Raman images of a diyne-SM/DOPC/chol ternary monolayer (1:1:1 molar ratio) on a quartz substrate. The images were reconstructed based on (*A*) the intensity of the diyne peak at 2,264 cm^{-1} and (*B*) that of the peak bottom at 2,222 cm^{-1}. The images consist of 54 × 28 pixels. (Scale bar: 10 μm.)

similar to that of the diyne-SM monolayer (Fig. 4*D* and Fig. S4). A characteristic peak of chol at 2,936 cm^{-1} was also observed in the ordered domains (Fig. S4), suggesting a higher content of chol as well as diyne-SM. However, the peak profile at the disordered domain (Fig. 4*D*) was similar to that of the DOPC monolayer (Fig. S4). The spatial distribution of Raman spectra along the yellow line in Fig. 4*A* was reconstructed, and the position-dependent change of the peak profile of CH_2/CH_3 stretching corresponded well to the intensity change of the diyne peak (Fig. 4*E*).

High-resolution Raman imaging was performed to visualize the distribution of diyne-SM inside a raft-like ordered domain of the ternary monolayer (Fig. 5*A*). We used slit-scanning Raman microscopy, which used a line-shaped laser focus for parallel Raman spectroscopic detection (16). Because the imaging speed of the slit-scanning configuration is more than 100 times faster than that of the point-scanning configuration, we could increase the image pixel number to observe fine structure in the sample. The Raman image in Fig. 5*A* shows a heterogeneous distribution of diyne-SM within the round-shaped ordered domains; diyne-SM was enriched in the central area of the domain compared with the peripheral area. We also performed Raman imaging of pure diyne-SM monolayer by using slit-scanning Raman microscopy and confirmed the uniform intensity distribution of the image (Fig. S5). The fluorescence image of the ternary monolayer containing 0.2 mol% Bodipy-PC was also obtained (Fig. 5*B*, *Lower*, and Fig. S6*A*), in which the ordered domains appeared as dark areas. A Raman image of the diyne peak at 2,264 cm^{-1} at the same area of the same sample was also obtained (Fig. 5*B*, *Upper*, and Fig. S6*B*) to compare the two imaging modalities. Diyne-SM was observed as round-shaped domains showing inverted contrast with respect to the fluorescence image. The dark regions in the fluorescence image overlap well with the bright regions in the Raman image (Fig. S6*C*), which is in accordance with the previous finding that Bodipy-PC is preferentially localized in the disordered domain (7, 8). This result also supports the idea that diyne-SM is preferentially incorporated into the ordered domain. The line profiles of Raman and fluorescence images were taken (Fig. 5*C*). The fluorescence image shows a dip at ordered domains, and larger domains have a flat bottom, indicating that fluorescent probe cannot reach the center of the domains. However, the Raman image shows protrusions rather than trapezoidal peaks, which should represent the distribution of diyne-SM in the ordered domain; the results in Fig. 5 confirm that the alkyne tag directly reflected the contents of a specific lipid constituent in the raft-like ordered domains, which is usually impossible with fluorescence probes.

The influence of substitution of SM with the diyne moiety should be carefully considered, because it may potentially alter the membrane properties. Among various parameters, the interactions between SM-SM and SM-chol are thought to be a pivotal driving force for phase segregation and ordered domain formation (21, 22). We, therefore, investigated the interaction between SM and chol or diyne-SM and chol using differential scanning calorimetry (DSC) and surface pressure-area isotherm (π-*A* isotherm) measurements. DSC of pure SM and diyne-SM bilayers revealed values of the main transition temperature (T_m) of 44.5 °C and 39.5 °C, respectively (arrows in Fig. S7); a similar drop in T_m values was reported for perdeuterated PC (d_{62}-dipalmitoyl-PC), which was previously used as a Raman probe (23). The π-*A* isotherms of diyne-SM/chol and SM/chol binary monolayers are shown in Fig. 6 *A* and *B*. Pure diyne-SM and pure SM monolayers showed phase transition from liquid-expanded (LE) to liquid-condensed phase at 20–30 and 10–20 mN/m, respectively (black lines in Fig. 6 *A* and *B*). To evaluate the influence of chol on the molecular packing of the SMs, the mean molecular areas (A_{mean}) were plotted as a function of the molar fraction of chol (x_{chol}) at 5 mN/m (Fig. 6 *C* and *D*), where pure diyne-SM and SM monolayers form homogeneous LE phase. The lateral molecular area of SM at 5 mN/m (61 $Å^2$) is close to that in the fluid-phase bilayer (57 $Å^2$), which was calculated from the molecular volume (1,225 $Å^3$) and bilayer thickness (43 Å) (24). In both the diyne-SM/chol and the SM/chol mixtures, the A_{mean} values were smaller than the additive functions over all of the experimental x_{chol} range, suggesting the existence of similar intermolecular condensation in the diyne-SM/chol and SM/chol monolayers. For additional analysis, we calculated the partial molecular area (PMA) of chol A_{PMA} by fitting the data to two linear functions according to a previous report (25). Similar A_{PMA} values were obtained for diyne-SM/chol (−7 ± 5 $Å^2$) and SM/chol (−3 ± 5 $Å^2$) monolayers at lower concentrations of chol (Fig. 6*E*). Assuming that the lateral area of rigid chol is constant at 38 ± 1 $Å^2$, irrespective of composition, these results suggest that the chol-induced condensation of diyne-SM is similar to that of SM at lower concentrations of chol. The A_{PMA} values increased to ~40 $Å^2$ at similar compositions: at $x_{chol} = 0.37$ for diyne-SM/chol and $x_{chol} = 0.35$ for SM/chol. These x_{chol} values, called break points, are likely to correspond to the composition at which all monolayer domains transform completely into the ordered phase; the same analysis and interpretation have been applied to the L_d/L_o phase transition in SM/chol bilayer systems (26). Because the A_{PMA} value above the break point is consistent with the lateral occupied area of pure chol (~38 ± 1 $Å^2$), no condensation of SM occurs above the break point, and thus, the capacity for chol should be similar between diyne-SM and SM. Direct evidence for the chol-induced condensation of SM could be obtained by membrane rigidity and areal compressional modulus C_s^{-1} analysis. For both the diyne-SM/chol and the SM/chol monolayers, the C_s^{-1} values of the diyne-SM/chol and SM/chol monolayers were in line with the theoretical curves (27) below each break point (solid lines in Fig. 6 *F* and *G*). However, additional increase

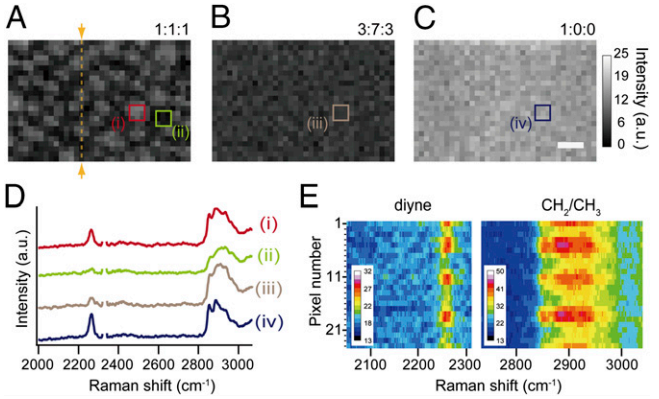

Fig. 4. Raman images of diyne-SM/DOPC/chol ternary monolayers with composition ratios of (*A*) 1:1:1, (*B*) 3:7:3, and (*C*) 1:0:0 reconstructed using the intensity of the diyne peak at 2,263 cm^{-1}. (*D*) Averaged Raman spectra from rectangular areas marked *i*–*iv* in *A*–*C*. Area *i* corresponds to an ordered domain, whereas area *ii* corresponds to a disordered region. Each rectangular area includes 9 (3 × 3) pixels. The Raman peak of N_2 at 2,330 cm^{-1} was removed so that the diyne peak could be clearly seen. (*E*) Spatial distribution of Raman spectra of the diyne-SM/DOPC/chol ternary monolayer at a 1:1:1 ratio acquired along the yellow line marked in *A*. Wavenumber region includes the diyne peak and CH_2/CH_3 stretching vibrational mode. The images consist of 36 × 24 pixels. (Scale bar: 10 μm.)

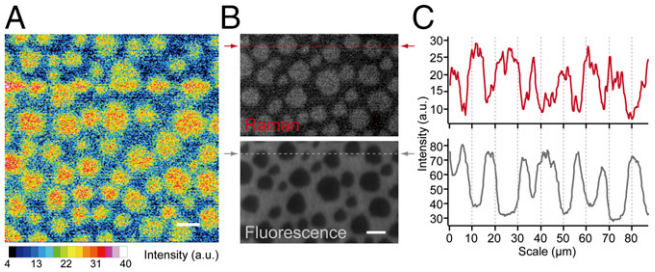

Fig. 5. (*A*) High-resolution Raman imaging of a 1:1:1 diyne-SM/DOPC/chol ternary monolayer taken with slit-scanning Raman microscopy. The image was reconstructed using the diyne peak intensity at 2,262 cm^{-1}. Exposure time and laser power were 100 s per line and 10.5 $mW/\mu m^2$. The image is shown in a 16-color display. The images consist of 412 × 400 pixels. (Scale bar: 10 μm.) (*B*) Raman and fluorescence images of a 1:1:1 diyne-SM/DOPC/chol ternary monolayer containing 0.2 mol% Bodipy-PC. Raman and fluorescence images were obtained in the same imaging area of the same sample. The Raman image was reconstructed using the diyne peak intensity at 2,264 cm^{-1}. The fluorescence image was reconstructed using the average fluorescence intensity at 542–603 nm. Fluorescence background during Raman imaging was suppressed by photobleaching of Bodipy-PC under 532-nm laser exposure. Exposure time and laser power for Raman imaging were 60 s per line and 14.1 $mW/\mu m^2$. Exposure time and laser power for fluorescence imaging were 0.5 s per line and 0.3 $mW/\mu m^2$. Each image consists of 387 × 250 pixels. (Scale bar: 10 μm.) (*C*) Line profiles of lipid rafts calculated along the dotted lines of the Raman and fluorescence images in *B* (red and gray, respectively). The line profile from the Raman image was smoothed using the moving average.

in chol concentration led to positive deviation of C_s^{-1} from the ideal function. On the basis of the results in Fig. 6 *F* and *G*, the molecular compressional modulus C_{mol}^{-1} of diyne-SM and SM turned out to be similar in the chol-absent LE and the chol-present ordered phases (Table 1). These results clearly indicate that the interaction properties of diyne-SM and SM with chol are closely similar.

Moreover, we compared the mobility and orientation of acyl chains of diyne-SM and SM in SM/DOPC/chol (1:1:1 mol:mol:mol) bilayers by means of ^2H NMR analysis (Fig. 7) of partly deuterated analogs (Fig. 7 *A* and *B*). The SM mixture gave two pairs of Pake doublets at $\Delta\nu = 51.9$ kHz and $\Delta\nu = 36.3$ kHz. The outer and inner Pake doublets correspond to the L_o and L_d domains, respectively (Fig. 7*C*) (28). The diyne-SM mixture gave a pair of Pake doublets at $\Delta\nu = 48.1$ kHz, which is close to the outer Pake obtained from the SM mixture ($\Delta\nu = 51.9$ kHz) (Fig. 7*D*); the inner doublet of the diyne-SM membrane was not clearly observed, probably because of a smaller content of L_d phase in the liposome preparation. Thus, the L_o phase developed in the diyne-SM ternary mixture in bilayer form showed similar mobility to that of SM.

Discussion

The heterogeneous distribution of diyne-SM in ordered domains, as seen in Fig. 5*A*, implies the existence of intermediate regions between SM-rich ordered and SM-poor disordered domains. This gradual change in the concentration of diyne-SM from the core to the peripheral areas of the SM-rich domain implies a slightly different view from that of the common raft model, in which the raft and nonraft phases show a relatively clear biphasic separation. According to previous atomic force microscope observations, the monolayer thickness is larger for the ordered domain than for the disordered domain because of the extension of acyl chains in the former domains (29). Considering that SM-induced intermolecular hydrogen bonding facilitates the ordering of lipid packing and increases membrane thickness, the intermediate region may possibly work to mitigate the thickness gap between the SM-rich and -poor domains, avoiding direct contact of these two regions. Because Raman imaging required relatively long acquisition times, we prepared the membrane on a quartz substrate using the LB technique. According to previous literature, the distribution of domains and the compositions of phases were usually preserved on the sample transfer from the water surface to a relatively hydrophilic substrate and also, unchanged for long time (30). Therefore, our Raman images are likely to be snapshots of the dynamic LB membrane on the water surface. Although the results in this study cannot be directly applied to biological membranes, the images indicate that the distribution of SM is not homogeneous, even in a single raft domain, which may have

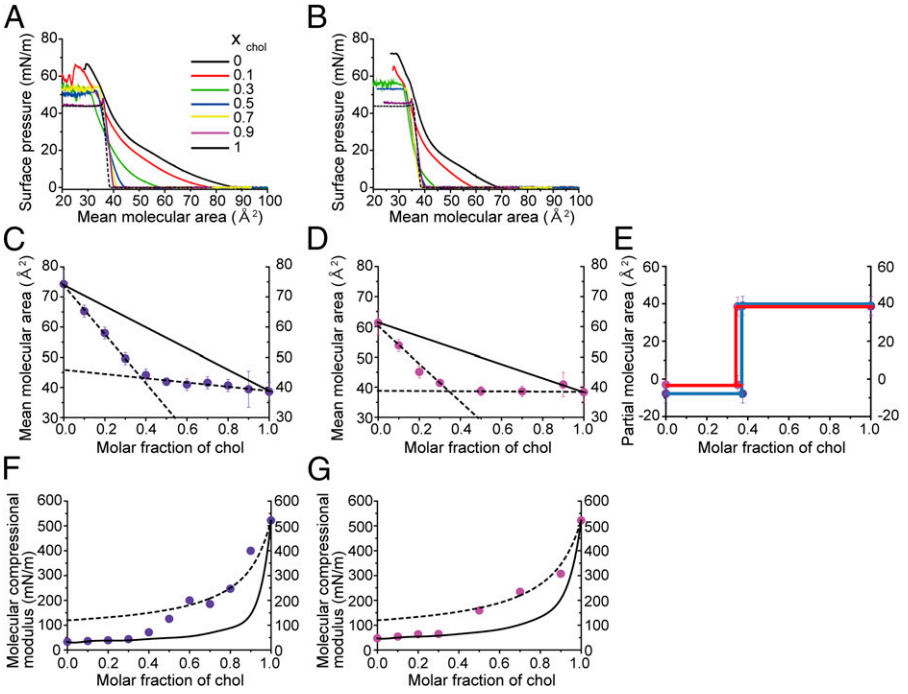

Fig. 6. Surface pressure vs. molecular area isotherms of (*A*) diyne-SM/chol and (*B*) SM/chol binary monolayers. Reported data for SM/chol mixtures in *B*, *D*, and *G* were redrawn for comparison (24). The molar fraction of chol x_{chol} is directly shown. The plots show mean molecular area A_{mean} vs. composition of (*C*) diyne-SM/chol and (*D*) SM/chol binary monolayers at 5 mN/m. Each result can be fitted to two lines as indicated by dashed lines. Theoretical mean molecular areas (additivity functions) are indicated by solid lines. (*E*) The PMAs A_{PMA} of chol in (blue) diyne-SM/chol and (red) SM/chol monolayers at 5 mN/m were estimated from *C* and *D*, respectively (27). The cross-sections between dashed lines and $x_{chol} = 1$ in *C* and *D* show A_{PMA} values, which are sums of the lateral areas occupied by chol and the chol-induced lateral expansion of neighboring lipids. (*F* and *G*) The molecular compressional modulus C_{mol}^{-1} of the diyne-SM and SM in the ordered phase was estimated by fitting the data to the theoretical function in the region of $x_{chol} \geq 0.5$ (dashed lines in *F* and *G*), in which all monolayer domains form the ordered phase. The cross-sections between $x_{chol} = 0$ and the dashed lines correspond to the values of C_{mol}^{-1} (24). The C_s^{-1} vs. composition plots are shown for (*F*) diyne-SM/chol and (*G*) SM/chol binary monolayers at 5 mN/m (27). The solid lines indicate the theoretical C_s^{-1} values of SM/chol mixtures, and the dashed lines were obtained by fitting the data to the theoretical equation in the region of $x_{chol} \geq 0.5$. Analysis is in *SI Materials and Methods*.

Table 1. Molecular compressional modulus of SM C_{mol}^{-1} in the diyne-SM/chol and SM/chol monolayers

	$x_{chol} = 0$ (LE phase; mN/m)	$x_{chol} \geqq 0.5$ (ordered phase; mN/m)
Diyne-SM	33 ± 10	120 ± 20
SM	47 ± 10	115 ± 20

The C_{mol}^{-1} values were calculated from Fig. 6 *F* and *G*; the cross-sectional values between the dashed curves and $x_{chol} = 0$ correspond to C_{mol}^{-1} in the ordered phase (24).

implications for the dynamic properties of lipid rafts with diverse lipid compositions in biomembranes. To elucidate the dynamic behavior of SM molecules in a biological membrane, additional improvement of the performance of Raman microscopy in terms of imaging speed and sensitivity will be an important next step.

We substituted a Raman tag at the head group of lipid to observe SM molecules bearing intrinsic acyl chains in the raft mixture. Perdeuterated acyl-chained lipids, such as those of d_{62}-dipalmitoyl-PC, have been often used as Raman-tagged lipid probes, because C–D bonds exhibit peaks in the silent region of biomolecules, and relatively strong Raman scattering occurs owing to the copious C–D bonds (23). This strategy is useful to examine head group effects on the phase behavior but is not ideal for investigating the interactions between acyl chains; deuterium labeling is known to slightly but significantly alter thermodynamic parameters, such as transition enthalpy, and also, influence phase behavior in single and multicomponent systems (23, 31). For the lipid head group, the number of sites available for introducing a Raman tag is relatively limited. Alkyne, particularly conjugated diyne, is a promising Raman tag for the head group because of its strong Raman intensity (18). We incorporated a conjugated diyne moiety into the ammonium group at the polar head and successfully recorded its image in an artificial monolayer with a raft-mimicking composition. It is important to examine the influence of modification of the head group with diyne on the membrane properties of SM. We quantitatively evaluated the membrane properties of diyne-SM and naturally occurring SM in the presence and absence of chol by using DSC, π-*A* isotherm measurements, and solid-state NMR. DSC revealed that the T_m of pure diyne-SM bilayer was 5 °C lower than that of SM, which is the same as the difference between PC and perdeuterated-PC (23). This correspondence implies that introduction of the diyne group into the SM head group perturbs lipid–lipid interactions to a similar extent as the case of perdeuteration of the acyl chains of PC. Areal and compressional modulus analysis further showed that the interactions between diyne-SM and chol are similar to those between SM and chol (Fig. 6*E* and Table 1). The NMR spectra of ternary mixtures showed that the mobility of the hydrocarbon chains of the d_2-diyne-SM (Fig. 7*B*) in the ordered phase is similar to that of d_2-SM (Fig. 7*A*) in the SM/DOPC/chol mixture (1:1:1 molar ratio) (Fig. 7). In addition, both of the fluorescence images of diyne-SM/DOPC/chol and SM/DOPC/chol monolayers in the presence of Bodipy-PC showed that the ordered domains with circular shape are separated from the disordered matrix (Fig. S8). Considering that the domain shape is sensitive to the environmental conditions, such as the membrane properties of the coexisting phases, phase equilibrium, and electrostatic force between lipid constituents (32), these results suggested that the diyne moiety hardly modulates the membrane properties and phase behavior.

As an imaging modality for lipid membranes, IR absorption spectroscopy shows high chemoselectivity, detecting molecular vibrations with higher sensitivity than Raman spectroscopy. However, the spatial resolution of IR absorption microscopy is restricted to micrometer scale owing to the long wavelength of the probe light (33). Raman microscopy, however, provides higher resolution with visible or near-IR excitation. Recently developed coherent Raman microscopy allows fast molecular imaging (34, 35). Lipid bilayer in lipid vesicles or supported membranes has been observed with coherent anti-Stokes Raman scattering microscopy (36, 37). Imaging of lipid monolayer, however, has not been achieved with this type of microscopy to our knowledge. Although it requires long imaging times, spontaneous Raman microscopy may have an advantage for observing low-concentration molecules, because image contrast of coherent Raman microscopy can be affected by signals that are not related to molecular vibration, such as nonresonant background or spurious background caused by cross-phase modulation. Secondary ion mass spectrometry (SIMS) is an emerging technique, in which lipid molecules on the substrate are bombarded with an ion beam, and lipid-specific fragment ions are analyzed by time-of-flight MS without labeling of target molecules (30, 38). Although this technique requires destructive imaging conditions, including ultrahigh vacuum, and suffers from a matrix effect that prevents quantitative analysis, it has been applied to molecule-specific imaging of raft mixtures (38). Quantitative analysis with SIMS was recently achieved by using a magnetic sector detection system (39, 40). This imaging modality achieves chemical specificity by using isotopic labeling of target molecules and affords high spatial resolution up to 50 nm. Chemoselective and quantitative imaging modalities based on MS are also expected to bring a new dimension to lipid raft research (41).

One of the disadvantages of Raman microscopy is its low sensitivity. Nevertheless, it has unique capabilities, including the observation of living organisms in aqueous and physiological environments (14, 15). In addition, intrinsic vibrational modes of membrane lipids in Raman spectra can provide a great deal of molecular information about the composition, structure, and phase state of lipid molecules (12). Furthermore, fluorescence imaging and Raman observation can be performed with the same sample in the same microscopic setup (Fig. 5 and Fig. S6), providing complementary information. In addition, Raman microscopy, in principle, can perform label-free imaging of lipid membranes by observing their intrinsic vibrational modes. As shown in Fig. 2, the peak profile of intrinsic CH_2/CH_3 stretching vibrations at 2,800–3,000 cm^{-1} varied depending on the lipid species. Detailed analysis using spectral unmixing (42) may enable us to discriminate the distributions of plural lipid components, potentially enabling label-free Raman observation of lipid rafts.

In conclusion, Raman microscopic observation of a raft-mimicking SM/DOPC/chol ternary monolayer was performed. We could specifically detect the distribution of SM tagged with a diyne group from the complicated Raman spectra of the lipid mixture. The membrane properties of diyne-SM were similar to those of naturally occurring SM, which was confirmed by DSC, π-*A* isotherm, and solid-state NMR. Raman intensity distribution, reconstructed from the Raman peak height of the diyne, clearly visualized segregated diyne-SM microdomains in the monolayer membrane, whereas such domains are usually observed as uniformly dark areas in fluorescence microscopy. We

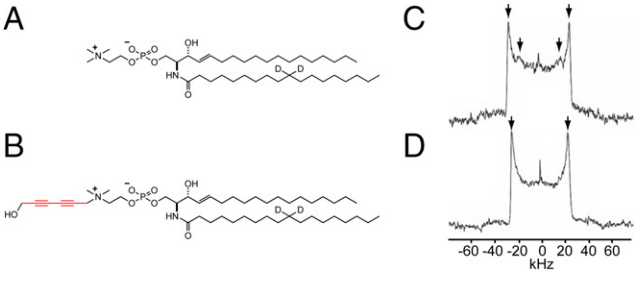

Fig. 7. Chemical structures of (*A*) d_2-SM and (*B*) d_2-diyne-SM and the NMR spectra of (*C*) d_2-SM/DOPC/chol and (*D*) d_2-diyne-SM/DOPC/chol (molar ratio of 1:1:1) ternary bilayers at 30 °C. The d_2-SM/DOPC/chol mixtures gave two Pake doublets at $\Delta\nu$ = 51.9 kHz (L_o) and $\Delta\nu$ = 36.3 kHz (L_d). The d_2-diyne-SM/DOPC/chol mixtures gave a single Pake doublet at $\Delta\nu$ = 48.1 kHz (L_o).

found that diyne-SM shows a heterogeneous distribution even inside raft-like ordered domains; it was enriched in the central area compared with peripheral areas. Our proposed alkyne-tag Raman imaging, performed in this study at single lipid-layer sensitivity, should be a useful tool for research on lipid membranes, especially lipid rafts, by providing both quantitative and molecule-specific chemical contrast with hyperspectral imaging capability.

Materials and Methods

Materials. Porcine brain SM and DOPC were purchased from Avanti Polar Lipids, and chol was purchased from Sigma Aldrich. SM with a saturated 18:0 acyl chain was extracted from brain SM and purified by HPLC. The purity of the SM was checked by MS and TLC. These lipids were separately dissolved in chloroform/methanol (4:1 vol/vol) at a concentration of 1 mg/mL and stored at −20 °C until use. A fluorescent probe, Bodipy-PC, was brought from Molecular Probes. This probe was dissolved in chloroform/methanol (4:1 vol/vol) at a concentration of 50 μg/mL and stored in the dark at −20 °C. Raman-tagged SM (diyne-SM) was newly synthesized (details in *SI Materials and Methods* and Figs. S9 and S10); d_2-diyne-SM was synthesized similarly to diyne-SM, and d_2-SM was prepared (details in Figs. S11 and S12), as reported (28). Other chemicals were purchased from Wako Pure Chemical Industries, Ltd.

Supported Monolayer Preparation. Monolayers of lipid mixtures were prepared on a computer-controlled Langmuir film balance (USI System) calibrated using stearic acid (Sigma Aldrich). The subphase, which consisted of distilled, freshly deionized water, was obtained using a Milli-Q System. The sample solution was prepared by mixing the appropriate amount of each lipid dissolved in chloroform/methanol (4:1 vol/vol) in a microvial. A total of 30 μL lipid solution (1 mg/mL) was spread onto the aqueous subphase (100 × 290 mm^2) using a glass micropipette (Drummond Scientific Company). After an initial delay period of 10 min for evaporation of the organic solvent, the monolayers were compressed at a rate of 20 mm^2/s. The subphase and ambient temperatures were controlled at 25.0 °C ± 0.1 °C and 25 °C ± 2 °C, respectively. A thin quartz plate was dipped horizontally into the water followed by compression of the sample at 20 mm^2/s to reach $\pi = 12$ mN/m. After compression, the quartz substrate was extracted from the water at a rate of 0.1 mm/s, and quartz-supported monolayers were formed.

Raman/Fluorescence Microscopy. Raman scattering and fluorescence images and spectra in Figs. 2–4 were obtained using laser-scanning Raman microscopy (Raman-11; Nanophoton) with a 532-nm excitation laser. The laser beam was focused to a point at the sample and scanned in 2D over a sample to acquire the Raman image. Raman scattering and fluorescence images in Fig. 5 were obtained using a home-built slit-scanning Raman microscope with a 532-nm excitation laser. The laser beam was focused to a line at the sample and scanned in 1D over a sample to acquire the Raman image.

Details of the experimental procedures for Raman/fluorescence imaging and spectroscopy, DSC, π-A isotherm measurements, ^{2}H measurements, and synthesis and characterization of diyne-SM are described in *SI Materials and Methods*.

ACKNOWLEDGMENTS. We thank Dr. Fuminori Sato, Associate Prof. Shigeru Matsuoka, and Assistant Prof. Yuichi Umegawa [Japan Science and Technology Agency (JST), Exploratory Research for Advanced Technology Lipid Active Structure Project, Osaka University] and Mr. Naoya Inazumi (School of Science, Osaka University) for their support for NMR measurements. We also thank Dr. Almar Palonpon (JST Exploratory Research for Advanced Technology Sodeoka Live Cell Chemistry Project, Osaka University) for his support for the analysis of Raman imaging data. We thank Dr. Taisuke Ota (Nanophoton) for technical support for the Raman microscope system. This work was partially supported by RIKEN, JST, Osaka University Photonics Advanced Research Center, and Japan Society for the Promotion of Science KAKENHI (Grant-in-Aid for Scientific Research) Grants 23710276 (to H.Y.) and 25242073 (to M.M.).

1. Simons K, Ikonen E (1997) Functional rafts in cell membranes. *Nature* 387(6633):569–572.
2. Lingwood D, Simons K (2010) Lipid rafts as a membrane-organizing principle. *Science* 327(5961):46–50.
3. Simons K, Gerl MJ (2010) Revitalizing membrane rafts: New tools and insights. *Nat Rev Mol Cell Biol* 11(10):688–699.
4. Veatch SL, Keller SL (2003) Separation of liquid phases in giant vesicles of ternary mixtures of phospholipids and cholesterol. *Biophys J* 85(5):3074–3083.
5. Ahmed SN, Brown DA, London E (1997) On the origin of sphingolipid/cholesterol-rich detergent-insoluble cell membranes: Physiological concentrations of cholesterol and sphingolipid induce formation of a detergent-insoluble, liquid-ordered lipid phase in model membranes. *Biochemistry* 36(36):10944–10953.
6. Edidin M (2003) The state of lipid rafts: From model membranes to cells. *Annu Rev Biophys Biomol Struct* 32:257–283.
7. Korlach J, Schwille P, Webb WW, Feigenson GW (1999) Characterization of lipid bilayer phases by confocal microscopy and fluorescence correlation spectroscopy. *Proc Natl Acad Sci USA* 96(15):8461–8466.
8. Klymchenko AS, Kreder R (2014) Fluorescent probes for lipid rafts: From model membranes to living cells. *Chem Biol* 21(1):97–113.
9. Shaw JE, et al. (2006) Correlated fluorescence-atomic force microscopy of membrane domains: Structure of fluorescence probes determines lipid localization. *Biophys J* 90(6):2170–2178.
10. Yamaji A, et al. (1998) Lysenin, a novel sphingomyelin-specific binding protein. *J Biol Chem* 273(9):5300–5306.
11. Harder T, Scheiffele P, Verkade P, Simons K (1998) Lipid domain structure of the plasma membrane revealed by patching of membrane components. *J Cell Biol* 141(4):929–942.
12. Parker FS (1983) *Applications of Infrared, Raman, and Resonance Raman Spectroscopy in Biochemistry. Model Membranes, Biomembranes, and Lipid-Containing Systems* (Springer, Heidelberg), pp 421–478.
13. Sweetenham CS, Notingher I (2010) Raman spectroscopy methods for detecting and imaging supported lipid bilayers. *Journal of Spectroscopy* 24(1–2):113–117.
14. Hamada K, et al. (2008) Raman microscopy for dynamic molecular imaging of living cells. *J Biomed Opt* 13(4):044027.
15. Okada M, et al. (2012) Label-free Raman observation of cytochrome c dynamics during apoptosis. *Proc Natl Acad Sci USA* 109(1):28–32.
16. Palonpon AF, et al. (2013) Raman and SERS microscopy for molecular imaging of live cells. *Nat Protoc* 8(4):677–692.
17. Yamakoshi H, et al. (2011) Imaging of EdU, an alkyne-tagged cell proliferation probe, by Raman microscopy. *J Am Chem Soc* 133(16):6102–6105.
18. Yamakoshi H, et al. (2012) Alkyne-tag Raman imaging for visualization of mobile small molecules in live cells. *J Am Chem Soc* 134(51):20681–20689.
19. Yuan C, Furlong J, Burgos P, Johnston LJ (2002) The size of lipid rafts: An atomic force microscopy study of ganglioside GM1 domains in sphingomyelin/DOPC/cholesterol membranes. *Biophys J* 82(5):2526–2535.
20. Lawrence JC, Saslowsky DE, Edwardson JM, Henderson RM (2003) Real-time analysis of the effects of cholesterol on lipid raft behavior using atomic force microscopy. *Biophys J* 84(3):1827–1832.
21. Schmidt CF, Barenholz Y, Thompson TE (1977) A nuclear magnetic resonance study of sphingomyelin in bilayer systems. *Biochemistry* 16(12):2649–2656.
22. Bittman R, Kasireddy CR, Mattjus P, Slotte JP (1994) Interaction of cholesterol with sphingomyelin in monolayers and vesicles. *Biochemistry* 33(39):11776–11781.
23. Mendelsohn R, Koch CC (1980) Deuterated phospholipids as Raman spectroscopic probes of membrane structure. Phase diagrams for the dipalmitoyl phosphatidylcholine(and its d62 derivative)-dipalmitoyl phosphatidylethanolamine system. *Biochim Biophys Acta* 598(2):260–271.
24. Kinoshita M, Goretta S, Tsuchikawa H, Matsumori N, Murata M (2013) Characterization of the ordered phase formed by sphigomyelin analogues and cholesterol binary mixtures. *Biophysics (Oxf)* 9:37–49.
25. Edholm O, Nagle JF (2005) Areas of molecules in membranes consisting of mixtures. *Biophys J* 89(3):1827–1832.
26. Greenwood AI, Tristram-Nagle S, Nagle JF (2006) Partial molecular volumes of lipids and cholesterol. *Chem Phys Lipids* 143(1-2):1–10.
27. Ali S, Smaby JM, Brockman HL, Brown RE (1994) Cholesterol's interfacial interactions with galactosylceramides. *Biochemistry* 33(10):2900–2906.
28. Matsumori N, et al. (2012) Comprehensive molecular motion capture for sphingomyelin by site-specific deuterium labeling. *Biochemistry* 51(42):8363–8370.
29. Johnston LJ (2007) Nanoscale imaging of domains in supported lipid membranes. *Langmuir* 23(11):5886–5895.
30. Leufgen KM, Rulle H, Benninghoven A, Sieber M, Galla H-J (1996) Imaging time-of-flight secondary ion mass spectrometry allows visualization and analysis of coexisting phases in Langmuir-Blodgett films. *Langmuir* 12(7):1708–1711.
31. Guard-Friar D, Chen CH, Engle AS (1985) Deuterium isotope effect on the stability of molecules: Phospholipids. *J Phys Chem* 89(9):1810–1813.
32. McConnell HM, Tamm LK, Weis RM (1984) Periodic structures in lipid monolayer phase transitions. *Proc Natl Acad Sci USA* 81(10):3249–3253.
33. Lasch P, Naumann D (2006) Spatial resolution in infrared microspectroscopic imaging of tissues. *Biochim Biophys Acta* 1758(7):814–829.
34. Zumbusch A, Langbein W, Borri P (2013) Nonlinear vibrational microscopy applied to lipid biology. *Prog Lipid Res* 52(4):615–632.
35. Zhang D, Wang P, Slipchenko MN, Cheng J-X (2014) Fast vibrational imaging of single cells and tissues by stimulated Raman scattering microscopy. *Acc Chem Res* 47(8):2282–2290.
36. Potma EO, Xie XS (2005) Direct visualization of lipid phase segregation in single lipid bilayers with coherent anti-Stokes Raman scattering microscopy. *ChemPhysChem* 6(1):77–79.
37. Li L, Wang H, Cheng J-X (2005) Quantitative coherent anti-Stokes Raman scattering imaging of lipid distribution in coexisting domains. *Biophys J* 89(5):3480–3490.
38. McQuaw CM, Zheng L, Ewing AG, Winograd N (2007) Localization of sphingomyelin in cholesterol domains by imaging mass spectrometry. *Langmuir* 23(10):5645–5650.
39. Kraft ML, Weber PK, Longo ML, Hutcheon ID, Boxer SG (2006) Phase separation of lipid membranes analyzed with high-resolution secondary ion mass spectrometry. *Science* 313(5795):1948–1951.
40. Lozano MM, et al. (2013) Colocalization of the ganglioside G(M1) and cholesterol detected by secondary ion mass spectrometry. *J Am Chem Soc* 135(15):5620–5630.
41. Frisz JF, et al. (2013) Direct chemical evidence for sphingolipid domains in the plasma membranes of fibroblasts. *Proc Natl Acad Sci USA* 110(8):E613–E622.
42. Bergner N, et al. (2012) Unsupervised unmixing of Raman microspectroscopic images for morphochemical analysis of non-dried brain tumor specimens. *Anal Bioanal Chem* 403(3):719–725.

Supporting Information

Ando et al. 10.1073/pnas.1418088112

SI Materials and Methods

Experimental Procedures for Raman/Fluorescence Imaging and Spectroscopy.

Experimental procedures used for Fig. 2. Supported monolayer membranes of single lipid composition, including SM, diyne-SM, DOPC, and chol, were prepared on a quartz substrate (0.17-mm thickness; Starbar Japan), fixed in a metal chamber (Attofluor; Life Technologies), and placed on the sample stage of the microscope (Raman-11; Nanophoton). For Raman spectroscopic measurement, the 532-nm laser was focused at a point on the membrane with a water immersion objective lens (CFI Plan Apo IR 60XWI; Nikon). The laser intensity at the sample plane was 340 mW. Exposure time was 6 s. Slit width for the spectrophotometer was set as 50 μm. Raman measurement was performed 15 times at different positions on the same membrane. Averaged Raman spectra of each membrane are shown in Fig. 2. The Raman peak of diyne-SM appeared at 2,263 cm^{-1}.

Experimental procedures used for Fig. 3. Supported monolayer membrane of diyne-SM/DOPC/chol ternary monolayer with the composition ratio 1:1:1 was prepared on a quartz substrate (0.17-mm thickness; Starbar Japan). The membrane was fixed in a metal chamber (Attofluor; Life Technologies) and placed on the sample stage of the microscope (Raman-11; Nanophoton). For Raman spectroscopic measurement, the 532-nm laser was focused at a point on the membrane with a water immersion objective lens (CFI Plan Apo IR 60XWI; Nikon). Focus drift was suppressed during imaging by using a real-time feedback system (PFS; Nikon). The laser intensity at the sample plane was 360 mW. Exposure time was 6 s/pixel. Slit width for the spectrophotometer was set as 50 μm. Each Raman spectrum was smoothed using a moving average method. Raman images were reconstructed using peak intensity of diyne at 2,264 cm^{-1} and peak bottom intensity at 2,222 cm^{-1}. The Raman image of diyne was obtained after subtraction of the signal intensity between 2,264 and 2,222 cm^{-1}, whereas the Raman image of the peak bottom (2,222 cm^{-1}) was obtained after subtraction of the signal intensity between 2,222 and 2,180 cm^{-1}.

Experimental procedures used for Fig. 4. Supported monolayer membranes of diyne-SM/DOPC/chol ternary monolayer with composition ratios of 1:1:1, 3:7:3, and 1:0:0 were prepared on a quartz substrate (0.17-mm thickness; Starbar Japan). Each membrane on the substrate was fixed in a metal chamber (Attofluor; Life Technologies) and placed on the sample stage of the microscope (Raman-11; Nanophoton). For Raman spectroscopic measurement, a 532-nm laser was focused as a point on the membrane with a water immersion objective lens (UPLSAPO 60XW; Olympus). The laser intensity at the sample plane was 370 mW. Exposure time was 6 s/pixel. Slit width for the spectrophotometer was set as 50 μm. Smoothing of Raman data was done using a moving average. Raman images were reconstructed using peak intensity of diyne at 2,263 cm^{-1} after subtraction of peak bottom intensity.

Experimental procedures used for Fig. 5. The experimental setup was the same as used previously (1). Briefly, a frequency-doubled Nd:YVO_4 laser (Verdi; Coherent Inc.) was used as the excitation laser source. A line-shaped laser beam formed by a cylindrical lens was focused on the sample by a water immersion objective lens (CFI Plan Apo IR 60XWI; Nikon). Scattering light from the sample was collected by the same objective lens, chromatically separated by an edge filter (LP03-532RU-25; Semrock) to transmit Raman scattering light, and focused on the spectrophotometer slit (MK-300; Bunko Keiki) for detection with a cooled CCD camera (Pixis 400B; Princeton Instruments). Laser scanning was performed with a single-axis galvanometer mirror (710-745825, 000-3014016; GSI Lumonics).

For Raman imaging in Fig. 5*A*, a supported 1:1:1 ternary monolayer membrane of diyne-SM/DOPC/chol was prepared on a quartz substrate (0.17-mm thickness; Starbar Japan). The membrane on the substrate was fixed in a metal chamber (Attofluor; Life Technologies) and placed on the sample stage of the home-built slit-scanning Raman microscope. For Raman spectroscopic measurement, a 532-nm laser was focused as a line on the membrane with a water immersion objective lens (CFI Plan Apo IR 60XWI; Nikon). Focus drift was suppressed during imaging by using a real-time feedback system (PFS; Nikon). The laser intensity at the sample plane was 10.5 mW/$μm^2$. Exposure time was 100 s per line. Slit width for the spectrophotometer was set as 50 μm. The scanning number was 240 lines for Raman imaging, with an image size of 240 × 400 pixels. For noise reduction, the obtained Raman data were subjected to singular value decomposition (SVD) (1). We used a spectral region (1,799–2,301 cm^{-1}) in the calculation procedure of SVD. We chose four loading vectors that significantly contributed to the image contrast. After SVD processing, Raman images were reconstructed using the peak intensity of diyne at 2,262 cm^{-1} based on the averaged peak top intensity between 2,259 and 2,265 cm^{-1} after subtraction of the averaged peak bottom intensity between 2,223 and 2,229 cm^{-1}. To compensate for aspect ratio, the image in the scanning (horizontal) direction was extended 1.72 times by linear interpolation. The final image consists of 412 × 400 pixels.

For Raman and fluorescence imaging in Fig. 5*B*, a supported 1:1:1 ternary monolayer membrane of diyne-SM/DOPC/chol containing 0.2 mol% Bodipy-PC was prepared on a quartz substrate (0.17-mm thickness; Starbar Japan). The membrane on the substrate was fixed in a metal chamber (Attofluor; Life Technologies) and placed on the sample stage of the home-built slit-scanning Raman microscope. For both Raman and fluorescence imaging, a 532-nm laser was focused as a line on the membrane with a water immersion objective lens (CFI Plan Apo IR 60XWI; Nikon). First, fluorescence imaging was performed, and second, Raman imaging was performed at the same area of the same sample. Fluorescence background was suppressed during Raman imaging by photobleaching of Bodipy-PC under 532-nm laser exposure. Focus drift was suppressed during imaging by using a real-time feedback system (PFS; Nikon). The laser intensity at the sample plane was 14.1 mW/$μm^2$, and the exposure time was 60 s per line for Raman imaging. The laser intensity for fluorescence imaging was 0.3 mW/$μm^2$, and the exposure time was 0.5 s per line. Slit width of the spectrophotometer was set as 50 μm. The scanning number was 225 lines for both Raman and fluorescence imaging, with the image size of 225 × 250 pixels. For noise reduction, the obtained Raman data were subjected to SVD. We used a spectral region (2,000–2,314 cm^{-1}) in the calculation procedure of SVD. We chose four loading vectors that significantly contributed to the image contrast. After SVD processing, the Raman image was reconstructed using the peak intensity of diyne at 2,264 cm^{-1} based on the averaged peak top intensity between 2,261 and 2,267 cm^{-1} after subtraction of the averaged peak bottom intensity between 2,225 and 2,231 cm^{-1}. Fluorescence images were reconstructed using average intensity at 542–603 nm. To compensate for aspect ratio, the image in the scanning (horizontal) direction was extended 1.72 times by linear interpolation. The final image consists of 387 × 250 pixels.

Line profiles in Fig. 5*C* were calculated from the average intensity of 4 pixels along the vertical direction, which is indicated

by a red dotted line in the Raman image in Fig. 5*B*, *Upper* and a gray dotted line in the fluorescence image in Fig. 5*B*, *Lower*. The profile from the Raman image was smoothed by use of the moving average.

Experimental procedures used for Fig. S5. In Fig. S5*A*, the experimental setup was the same as used in Fig. 5. For Raman imaging, a supported membrane of diyne-SM monolayer was prepared on a quartz substrate (0.17-mm thickness; Starbar Japan). The membrane on the substrate was fixed in a metal chamber (Attofluor; Life Technologies) and placed on the sample stage of the home-built slit-scanning Raman microscope. For Raman spectroscopic measurement, a 532-nm laser was focused as a line on the membrane with a water immersion objective lens (CFI Plan Apo IR 60XWI; Nikon). Focus drift was suppressed during imaging by using a real-time feedback system (PFS; Nikon). The laser intensity at the sample plane was 13.9 mW/μm^2. Exposure time was 60 s per line. Slit width for the spectrophotometer was set as 50 μm. The scanning number was 200 lines for Raman imaging, with an image size of 200 × 190 pixels. For noise reduction, the obtained Raman data were subjected to SVD (1). We used a spectral region (1,800–2,310 cm^{-1}) in the calculation procedure of SVD. We chose four loading vectors that significantly contributed to the image contrast. After SVD processing, Raman images were reconstructed using the peak intensity of diyne at 2,263 cm^{-1} based on the averaged peak top intensity between 2,260 and 2,266 cm^{-1} after subtraction of the averaged peak bottom intensity between 2,212 and 2,218 cm^{-1}. To compensate for aspect ratio, the image in the scanning (horizontal) direction was extended 1.72 times by linear interpolation. The final image consists of 344 × 190 pixels. In Fig. S5*B*, the image was extracted from lower left portion in Fig. 5*A*, which consist of 344 × 190 pixels. In Fig. S5*C*, line profiles were calculated from the average intensity of 7 pixels along the vertical direction, which is indicated by a dotted lines.

Experimental procedures used for Fig. S6. A supported monolayer membrane of 1:1:1 diyne-SM/DOPC/chol ternary monolayer containing 0.2 mol% Bodipy-PC was prepared on a quartz substrate (0.17-mm thickness; Starbar Japan). The membrane on the substrate was fixed in a metal chamber (Attofluor; Life Technologies) and placed on the sample stage of the microscope (Raman-11; Nanophoton). For both fluorescence and Raman spectroscopic measurement, a 532-nm laser was focused as a point on the membrane with a water immersion objective lens (CFI Plan Apo IR 60XWI; Nikon). Focus drift was suppressed during imaging by using a real-time feedback system (PFS; Nikon). For fluorescence imaging, the laser intensity at the sample plane was 0.5 mW, and the exposure time was 1 s/pixel. For Raman imaging, the laser intensity at the sample was 360 mW, and the exposure time was 6 s/pixel. First, fluorescence imaging was performed, and second, Raman imaging was performed at the same area of the same sample. Slit width for the spectrophotometer was set as 50 μm. For reconstruction of fluorescence images, average intensity between 555 and 605 nm was used. Smoothing of Raman data was done using a moving average. Raman images were reconstructed using peak intensity of diyne at 2,264 cm^{-1} after subtraction of peak bottom intensity.

DSC Thermograms of Diyne-SM Bilayers. The thermal-phase behavior of SM bilayers was examined with a nanodifferential scanning calorimeter (Calorimetry Science Corp.). Bilayer samples were prepared by a conventional method. Briefly, SM dissolved in chloroform/methanol (4:1) was dried under a flow of nitrogen and then, reduced pressure for at least 24 h. The resulting lipid film was dispersed into distilled and deionized water (Simplicity UV; Merck Millipore) and incubated for ∼30 min at 60 °C with intermittent vortexing. The final concentration was 2.47 mM. Then, 330 μL sample was placed in the DSC immediately before measurement. A scanning rate of 0.5 °C/min was used. The main transition temperatures of diyne-SM and SM bilayers were found to be 39.5 °C and 44.5 °C, respectively, as shown by the arrows in Fig. S7.

π-*A* Isotherm Measurements and Supported Monolayer Preparation. Monolayers of lipid mixtures were prepared on a computer-controlled Langmuir film balance (USI System) calibrated using stearic acid (Sigma Aldrich). The subphase, which consisted of distilled, freshly deionized water, was obtained using a Milli-Q System. The sample solution was prepared by mixing the appropriate amount of each lipid solution in a microvial. A total of 30 μL lipid dissolved in chloroform/methanol (4:1 vol/vol; 1 mg/mL) was spread onto the aqueous subphase (100 × 290 mm^2) using a glass micropipette (Drummond Scientific Company). After an initial delay period of 10 min for evaporation of the organic solvent, the monolayers were compressed at a rate of 20 mm^2/s. The subphase and ambient temperatures were controlled at 25.0 °C ± 0.1 °C and 25 °C ± 2 °C, respectively. The π-*A* isotherm measurements were repeated three to five times under the same conditions. These measurements provided the molecular area at a corresponding pressure within an error of ∼ ±1 Å^2. The influence of oxidation on the unsaturated chains at the air–water interface was checked by intentionally exposing pure SM and pure DOPC monolayers to air for 10–30 min before compression. The change in the isotherm after prolonged exposure of SM or DOPC monolayer to air was within the error described above.

Analysis. In Fig. 6, we evaluated the intermolecular interaction in lipid binary mixtures at the surface pressure of 5 mN/m on the basis of the deviations of experimentally obtained mean molecular areas (A_{mean}) from those of ideal mixtures (A_{12}):

$$A_{12} = A_1(1-x) + A_2 x,$$

where A_1 and A_2 are the molecular areas of pure components 1 and 2 (e.g., SM and chol), respectively, and x is the molar fraction of component 2. Thus, the value of A_{12} corresponds to the mean molecular area in the mixture constituted of noninteractive or completely immiscible molecules. According to previous literature (2), PMAs of components 1 (A^1_{PMA}) and 2 (A^2_{PMA}) can be defined as

$$A^1_{\mathrm{PMA}} = \left(\frac{\partial N A^1_{\mathrm{mean}}}{\partial N_1}\right)$$

and

$$A^2_{\mathrm{PMA}} = \left(\frac{\partial N A^2_{\mathrm{mean}}}{\partial N_2}\right),$$

where N, N_1, and N_2 are the total amounts of all constituents and components 1 and 2, respectively. On the basis of the additivity rule, the A_{mean} also can be expressed as

$$A_{\mathrm{mean}}(x) = (1-x)A^1_{\mathrm{PMA}}(x) + xA^2_{\mathrm{PMA}}(x).$$

Here, denoting derivatives with respect to x by prime yields, the following equations are obtained:

$$A^1_{\mathrm{PMA}}(x) = A_{\mathrm{mean}}(x) - xA'_{\mathrm{mean}}(x)$$

and

$$A^2_{\mathrm{PMA}}(x) = A_{\mathrm{mean}}(x) + (1-x)A'_{\mathrm{mean}}(x).$$

Areal compressibility (C_s) at the surface pressure of 5 mN/m was calculated from the π-A isotherm using

$$C_s = -\frac{1}{A_{mean}}\left(\frac{\partial A_{mean}}{\partial \pi}\right)_{\pi}.$$

The compressibility in ideal mixtures (C_{12}) is calculated according to Ali et al. (3):

$$C_{12} = \left(\frac{1}{A_{12}}\{(C_{s1}A_1)(1-x) + (C_{s2}A_2)x\}\right),$$

where C_{s1} and C_{s2} are the areal compressibilities of the pure components 1 and 2, respectively. They suggested that C_{12} is additive with respect to the product of C_{si} and A_i rather than C_{si} for either ideal or completely nonideal mixing. Areal compressibility (C_s) was expressed in term of areal compressional modulus (C_s^{-1}) for easy comparison with previous data.

Fluorescence Observation of Ordered Domains in Diyne-SM/DOPC/Chol and SM/DOPC/Chol Ternary Monolayers. Fig. S8 shows fluorescence images of diyne-SM/DOPC/chol (1:1:1 mol/mol/mol) (Fig. S8*A*) and SM/DOPC/chol (1:1:1 mol/mol/mol) (Fig. S8*B*) quartz-supported monolayers in the presence of 0.2 mol% Bodipy-PC at 12 mN/m and 25 °C. Fluorescence observations were conducted using a confocal laser-scanning microscope (FV1000-D IX81; Olympus) with an air objective lens with a long working distance (LUCPLFLN 60X; Olympus). A wavelength of 488 nm was used for excitation of Bodipy. A laser-scanning rate of 4.0 or 8.0 μs/pixel was used for acquisition of confocal images (1,024 × 1,024 pixels).

^{2}H NMR Measurements. A mixture of lipids comprising 10.0 μmol d_2-SM or d_2-diyne-SM (Fig. 7), 10.0 μmol chol, and 10.0 μmol DOPC was dissolved in chloroform/methanol (1:1 vol/vol). After removing the solvent in vacuo for 20 h, the dried membrane film was hydrated with 1 mL distilled water and vigorously vortexed at 65 °C to make multilamellar vesicles. The sample was frozen and thawed three times, lyophilized, and rehydrated with deuterium-depleted water to make 50% (wt/wt) water. Then, the mixture was again frozen and thawed 10 times. The sample was transferred into a glass tube (5 × 26 mm), which was sealed with epoxy glue. ^{2}H NMR measurements were recorded on a 300-MHz CMX300 Spectrometer (Chemagnetics; Varian) with a 5-mm ^{2}H static probe (Otsuka Electronics) using a quadrupolar echo sequence (4). The 90° pulse width was 2 μs, interpulse delay was 30 μs, and repetition rate was 0.5 s. The sweep width was 200 kHz, and the number of scans was around 100,000.

General Information for the Synthesis of Diyne-SM. Chemicals and solvents were purchased from Nacalai Tesque, Aldrich, TCI, or Kanto Chemicals Inc. and used without additional purification unless otherwise noted. TLC was done on Merck Precoated Silica Gel 60 F-254 Plates. Spots on TLC plates were stained with phosphomolybdic acid. NMR spectra were collected on a JEOL ECA 500 (500 MHz) using deuterated solvent as the lock. Chemical shift is given in parts per million (δ), and coupling constant (J) is in hertz. The following terms are used to designate multiplicity: singlet (s), doublet (d), triplet (t), quartet (q), quintuplet (quint), multiplet (m), and broad (b). High-resolution mass spectra (HRMS) were recorded on an LTQ-Orbitrap XL.

Synthetic Procedures for Diyne-SM and d_2-Diyne-SM.

(2S,3R,E)-(2-stearoylamino-3-hydroxyoctadec-4-en-1-yl)-{2-[(6-hydroxyhexa-2,4-diyn-1-yl)dimethylammonio]ethyl}phosphate (diyne-SM). To a solution of propargyl alcohol **S1** (300 mg, 5.35 mmol) in acetone (15 mL), *N*-bromosuccinimide (1.02 g, 5.78 mmol) and silver nitrate (91 mg, 0.54 mmol) were added at room temperature. The reaction mixture was stirred at room temperature for 2 h and then, concentrated. The residue was extracted two times with diethyl ether. The combined organic layers were dried with Na_2SO_4, filtered, and concentrated to afford **S2** (645 mg, 90% yield) as a pale yellow oil, which was used directly in the next step. ^{1}H NMR (500 MHz, $CDCl_3$): δ 1.63 (brs, 1H), 4.30 (s, 2H). CuCl (0.3 mg, 3.1 μmol), *i*-$PrNH_2$ (5.1 μL, 0.06 mmol), and $NH_2OH{\cdot}HCl$ (1.0 mg, 14.5 μmol) were added to MeOH (1 mL) at room temperature under argon. The mixture was cooled to 0 °C, and then, **S3** (5) (compound **S3** was the intermediate for the synthesis of SM head group analogs; 40 mg, 0.05 mmol) was added, forming a yellow acetylide suspension. A solution of **S2** (21 mg, 0.16 mmol) in MeOH (0.2 mL) was added immediately. The reaction mixture was stirred at the same temperature for 30 min, concentrated, and extracted with $CHCl_3$. The combined organic layers were dried with Na_2SO_4, filtered, and concentrated. The mixture was passed through a short bed of silica gel eluting with $CHCl_3$/MeOH (5:1). The crude product was purified on a Cosmosil 5C18-AR-II column (10 × 150 mm; Nacalai Tesque) with MeOH as the eluent to give diyne-SM (5.1 mg, 12%) as a white solid. TLC: R_f = 0.18 (CH_2Cl_2/MeOH/NH_4OH 70:30:3); ^{1}H NMR (500 MHz, CD_3OD): δ 0.88 (t, J = 7.5 Hz, 6H); 1.24–1.42 (m, 50H); 1.53–1.63 (m, 2H); 2.01 (dt, J = 7.0, 7.0 Hz, 2H); 2.13–2.20 (m, 2H); 3.24 (s, 6H); 3.70 (t, J = 5.5 Hz, 2H); 3.87–3.98 (m, 2H); 4.03 (dd, J = 8.0, 8.0 Hz, 1H); 4.06–4.13 (m, 1H); 4.27 (s, 2H); 4.25–4.30 (m, 2H); 4.56 (s, 2H); 5.43 (ddt, J = 15.5, 8.0, 1.5 Hz, 1H); 5.69 (dtd, J = 15.5, 7.0, 1.0 Hz, 1H); 7.90 (d, J = 9.0 Hz, 1H); ^{13}C NMR (125 MHz, CD_3OD): δ 13.11, 22.41, 25.85, 29.15, 29.18, 29.37, 29.44, 29.74, 31.75, 32.15, 36.05, 49.55, 50.86, 53.93, 55.79, 58.90, 64.22, 64.61, 65.64, 66.54, 71.22, 75.42, 81.27, 129.89, 133.82, 174.58; HRMS (electrospray ionization) calculated for $C_{46}H_{86}N_2O_7P$ $[M + H]^+$ 809.6167, found 809.6184. ^{1}H and ^{13}C NMR spectra of diyne-SM are shown in Figs. S9 and S10. The synthetic scheme is summarized in Scheme S1.

(2S,3R,E)-[2-(10,10-dideuteriumstearoylamino)-3-hydroxyoctadec-4-en-1-yl]-{2-[(6-hydroxyhexa-2,4-diyn-1-yl)dimethylammonio]ethyl}phosphate (d_2-diyne-SM). This compound was prepared from **S4** (a full account of the synthesis of compound **S4** will be reported elsewhere) in 14% yield as a white solid by following the same procedure as described for **S3**. TLC: R_f = 0.18 (CH_2Cl_2/MeOH/NH_4OH 70:30:3); ^{1}H NMR (500 MHz, CD_3OD): δ 0.88 (t, J = 7.5 Hz, 6H); 1.22–1.43 (m, 48H); 1.50–1.63 (m, 2H); 2.01 (dt, J = 7.0, 7.0 Hz, 2H); 2.13–2.20 (m, 2H); 3.25 (s, 6H); 3.71 (t, J = 5.0 Hz, 2H); 3.88–3.99 (m, 2H); 4.02 (dd, J = 8.0, 8.0 Hz, 1H); 4.06–4.12 (m, 1H); 4.27 (s, 2H); 4.21–4.34 (m, 2H); 4.56 (s, 2H); 5.43 (ddt, J = 15.0, 8.0, 1.2 Hz, 1H); 5.69 (dtd, J = 15.0, 7.0, 0.6 Hz, 1H); 7.90 (d, J = 9.0 Hz, 1H); ^{13}C NMR (125 MHz, CD_3OD): δ 13.16, 22.43, 25.87, 29.18, 29.21, 29.33, 29.47, 29.52, 29.55, 29.58, 31.77, 31.79, 32.18, 36.06, 49.56, 50.87, 53.87, 53.93, 55.80, 58.90, 59.94, 64.22, 64.28, 64.61, 64.65, 65.67, 66.56, 71.21, 75.43, 81.29, 129.93, 133.79, 174.54; HRMS (electrospray ionization) calculated for $C_{46}H_{83}D_2N_2O_7PNa$ $[M + Na]^+$ 833.6112, found 833.6124. ^{1}H and ^{13}C NMR spectra of d_2-diyne-SM are shown in Figs. S11 and S12. Synthetic scheme is summarized in Scheme S2.

1. Palonpon AF, et al. (2013) Raman and SERS microscopy for molecular imaging of live cells. *Nat Protoc* 8(4):677–692.
2. Edholm O, Nagle JF (2005) Areas of molecules in membranes consisting of mixtures. *Biophys J* 89(3):1827–1832.
3. Ali S, Smaby JM, Brockman HL, Brown RE (1994) Cholesterol's interfacial interactions with galactosylceramides. *Biochemistry* 33(10):2900–2906.
4. Davis JH, Jeffrey KR, Bloom M, Valic MI, Higgs TP (1976) Quadrupolar echo deuteron magnetic resonance spectroscopy in ordered hydrocarbon chains. *Chem Phys Lett* 42(2):390–394.
5. Goretta SA, Kinoshita M, Mori S, Tsuchikawa H, Matsumori N, Murata M (2012) Effects of chemical modification of sphingomyelin ammonium group on formation of liquid-ordered phase. *Bioorg Med Chem* 20(13):4012–4019.

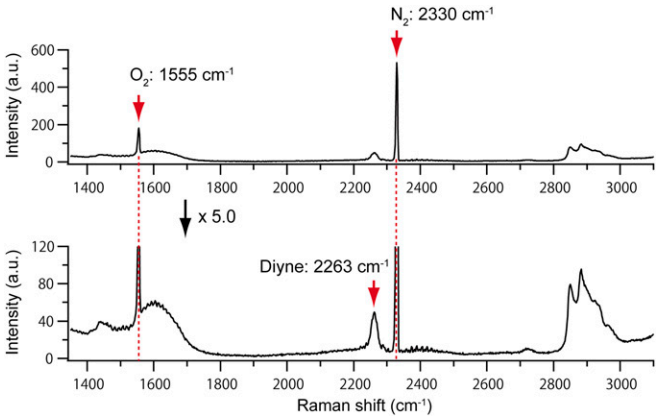

Fig. S1. Raman spectrum of the diyne-SM monolayer supported on a quartz substrate shown in Fig. 2*A*. Raman peaks of N_2, O_2, and diyne are indicated by red arrows. *Lower* is a five times enlarged view of *Upper* in terms of intensity (vertical axis). Strong Raman scattering by N_2 and O_2 in air was always detected during Raman measurement of lipid membranes. For ease of picking out the important Raman peaks, such as diyne, the two peaks of N_2 and O_2 have been removed in Figs. 2 and 4 and Figs. S3 and S4.

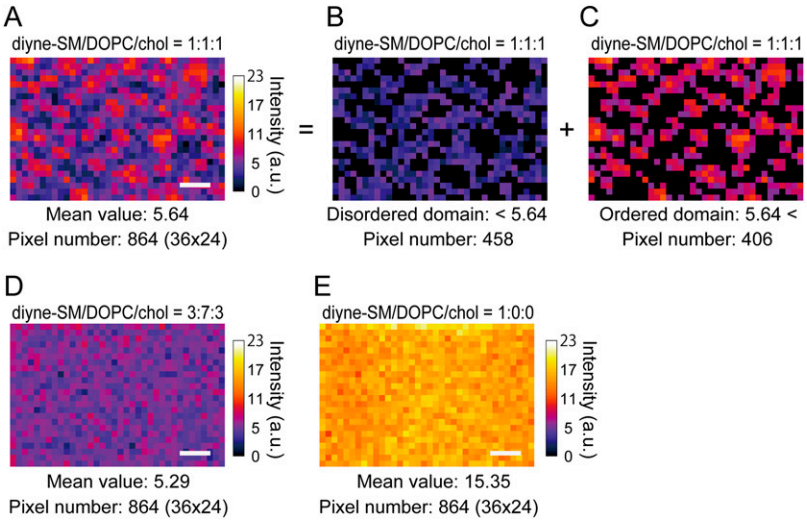

Fig. S2. (*A*) Raman image of the diyne-SM/DOPC/chol ternary monolayer with a 1:1:1 ratio reconstructed using the intensity of the diyne peak at 2,263 cm^{-1}. The image is the same as Fig. 4*A*. Mean value of the image is 5.64. The two phases were separated by taking pixel regions (*B*) below the mean value as disordered domains and (*C*) above the mean value as ordered domains. Raman images of diyne-SM/DOPC/chol ternary monolayers with (*D*) a 3:7:3 ratio and (*E*) a 1:0:0 ratio. The images are the same as Fig. 4 *B* and *C*, respectively. (Scale bar: 10 μm.)

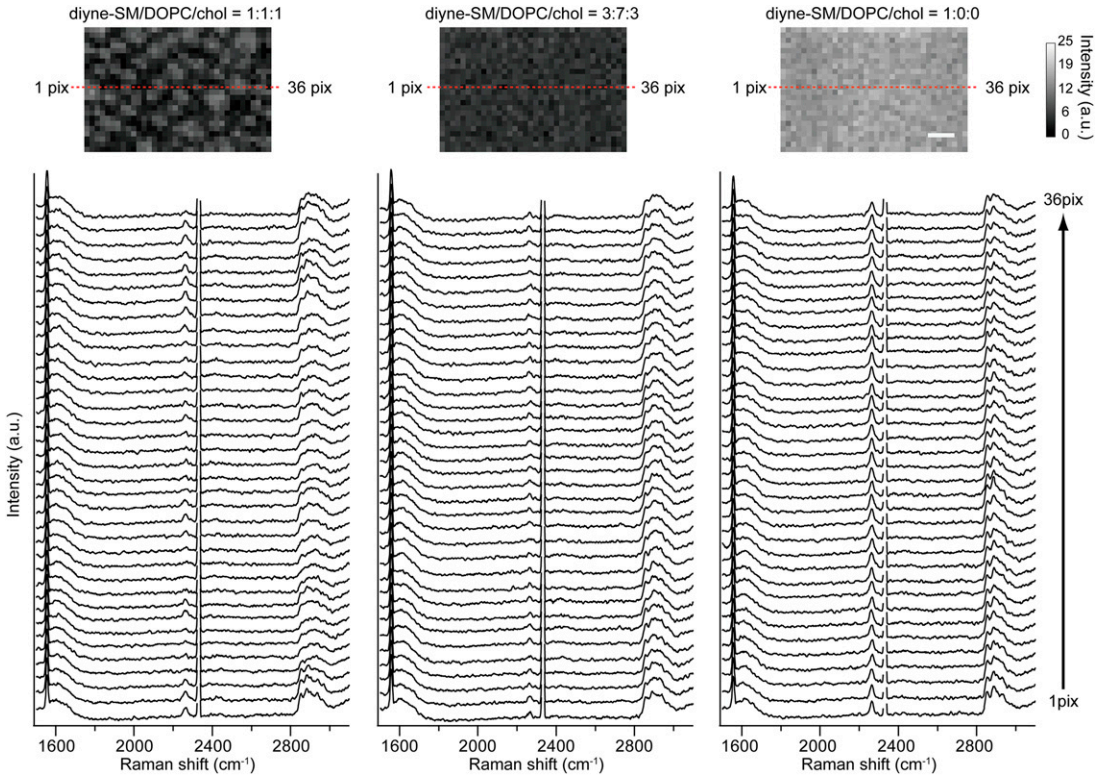

Fig. S3. Raman spectra obtained along the red lines in the Raman images of the diyne-SM/DOPC/chol ternary monolayer with 1:1:1, 3:7:3, and 1:0:0 ratios. The images are the same as in Fig. 4 *A*–*C*, with 36 × 24 pixels. Raman peak of N_2 at ~2,330 cm^{-1} was removed so that it would be easier to see Raman peaks from lipid molecules. Pix, pixel. (Scale bar: 10 μm.)

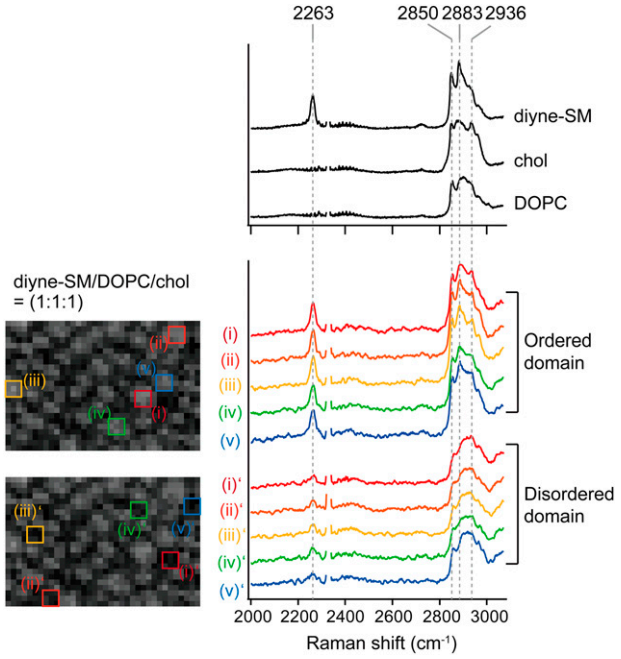

Fig. S4. Comparison between Raman spectra of supported lipid monolayers with single-component composition (diyne-SM, DOPC, or chol) and Raman spectra of diyne-SM/DOPC/chol ternary monolayer at ordered and disordered domains. The spectra of the ternary monolayer were obtained from five representative areas (3 × 3 pixels) calculated using the Raman image in Fig. 4*A*. Characteristic Raman peaks are displayed in the image, including diyne stretching vibration (2,263 cm^{-1}), CH_2 symmetric/asymmetric stretching vibration (2,850/2,883 cm^{-1}), and CH_3 symmetric stretching vibration (2,936 cm^{-1}). Raman peak of N_2 at ~2,330 cm^{-1} was removed so that it would be easier to see Raman peaks from lipid molecules.

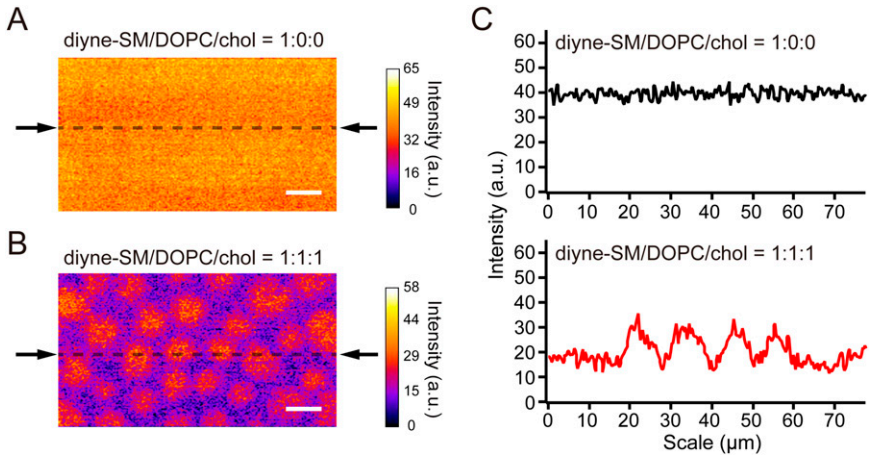

Fig. S5. (*A*) Raman image of a pure diyne-SM monolayer taken with slit-scanning Raman microscopy. The image was reconstructed using the diyne peak intensity at 2,263 cm^{-1}. Exposure time and laser power were 60 s per line and 13.9 $mW/\mu m^2$, respectively. The image consists of 344 × 190 pixels. (Scale bar: 10 μm.) (*B*) Raman image of a 1:1:1 diyne-SM/DOPC/chol ternary monolayer extracted from the lower left portion in Fig. 5*A*. The image consists of 344 × 190 pixels. (Scale bar: 10 μm.) (*C*) Line profiles of lipid membranes calculated along the dotted lines of the images in *A* and *B*.

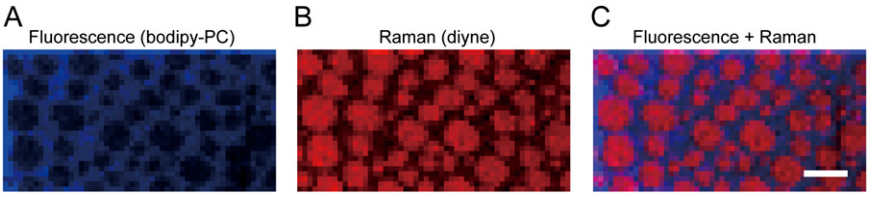

Fig. S6. (*A*) Fluorescence and (*B*) Raman images of a 1:1:1 diyne-SM/DOPC/chol ternary monolayer containing 0.2 mol% Bodipy-PC. The fluorescence image was reconstructed using the average fluorescence intensity at 555–605 nm (blue). The Raman image was reconstructed using the diyne peak intensity at 2,264 cm^{-1} (red). Both images were obtained in the same imaging area of the same sample. Fluorescence background during Raman imaging was suppressed by photobleaching of Bodipy-PC under 532-nm laser exposure. (*C*) Superimposed image of fluorescence and Raman images obtained in Fig. S5 *A* and *B*. The images consist of 54 × 28 pixels. (Scale bar: 20 μm.)

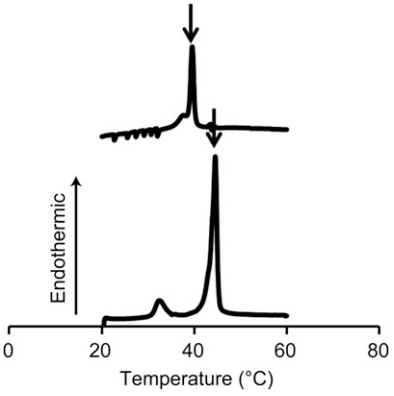

Fig. S7. DSC heating thermograms of (*Upper*) diyne-SM and (*Lower*) SM bilayers immediately after preparation. The main transitions are indicated by arrows.

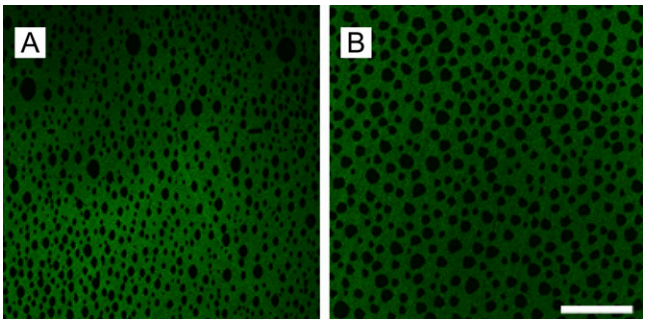

Fig. S8. Fluorescence images of (*A*) diyne-SM/DOPC/chol and (*B*) SM/DOPC/chol quartz-supported monolayers in the presence of 0.2 mol% Bodipy-PC at 12 mN/m and 25 °C. (Scale bar: 50 μm.)

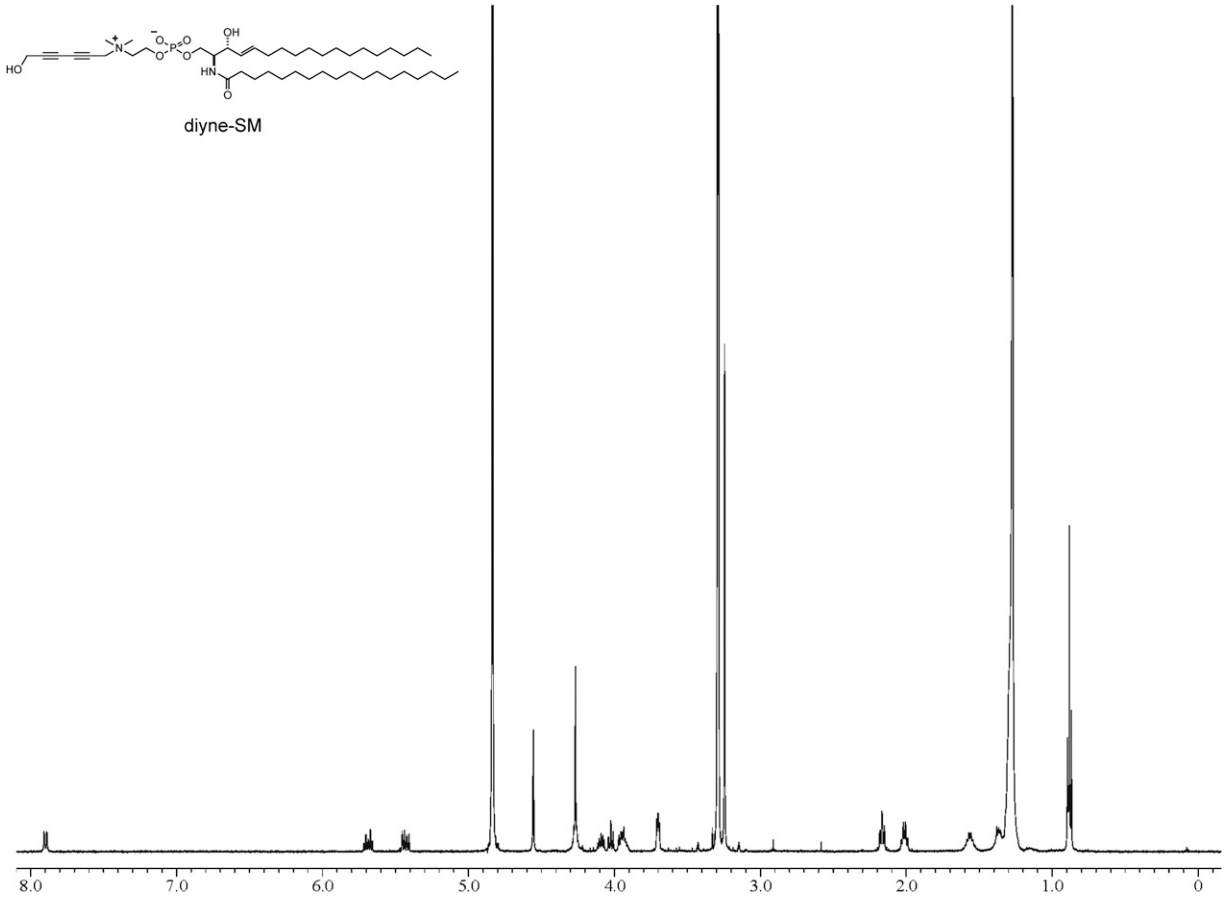

Fig. S9. ^{1}H NMR spectrum of diyne-SM.

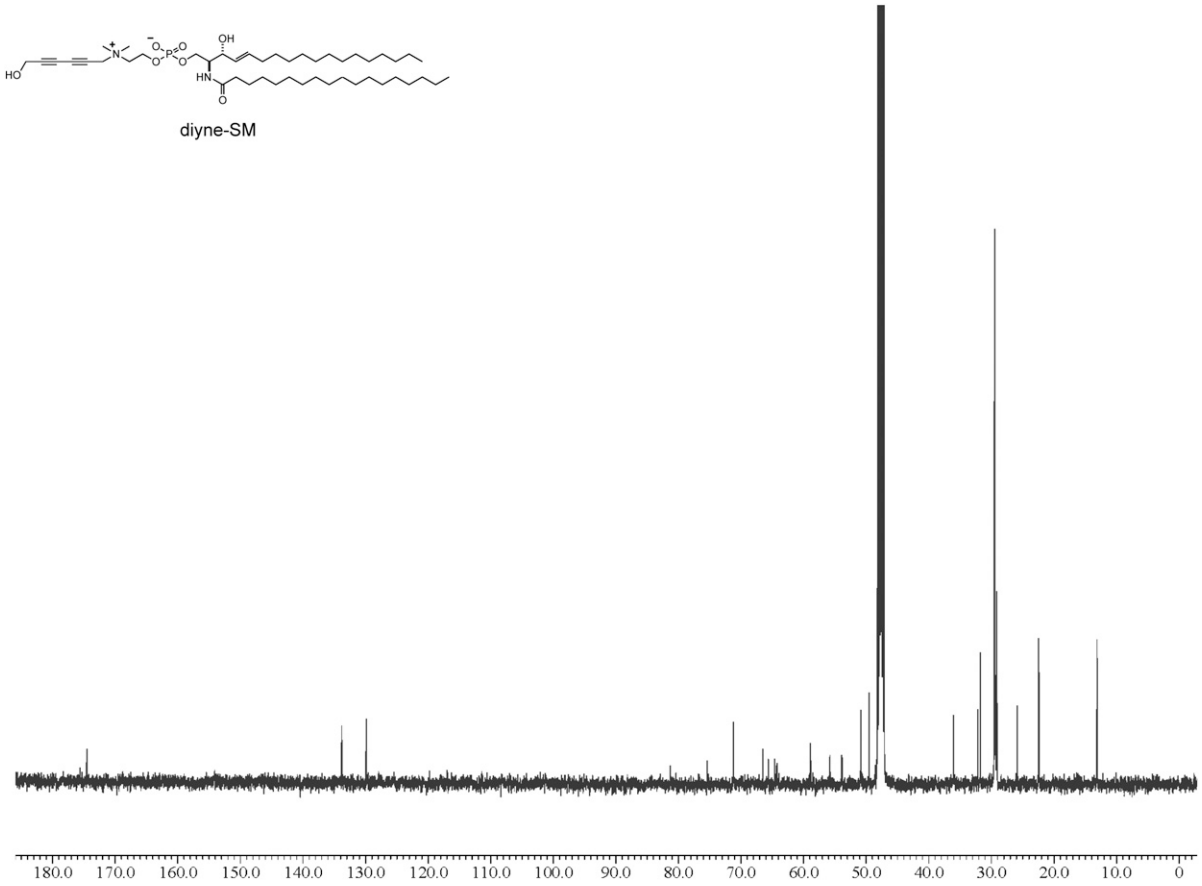

Fig. S10. ^{13}C NMR spectrum of diyne-SM.

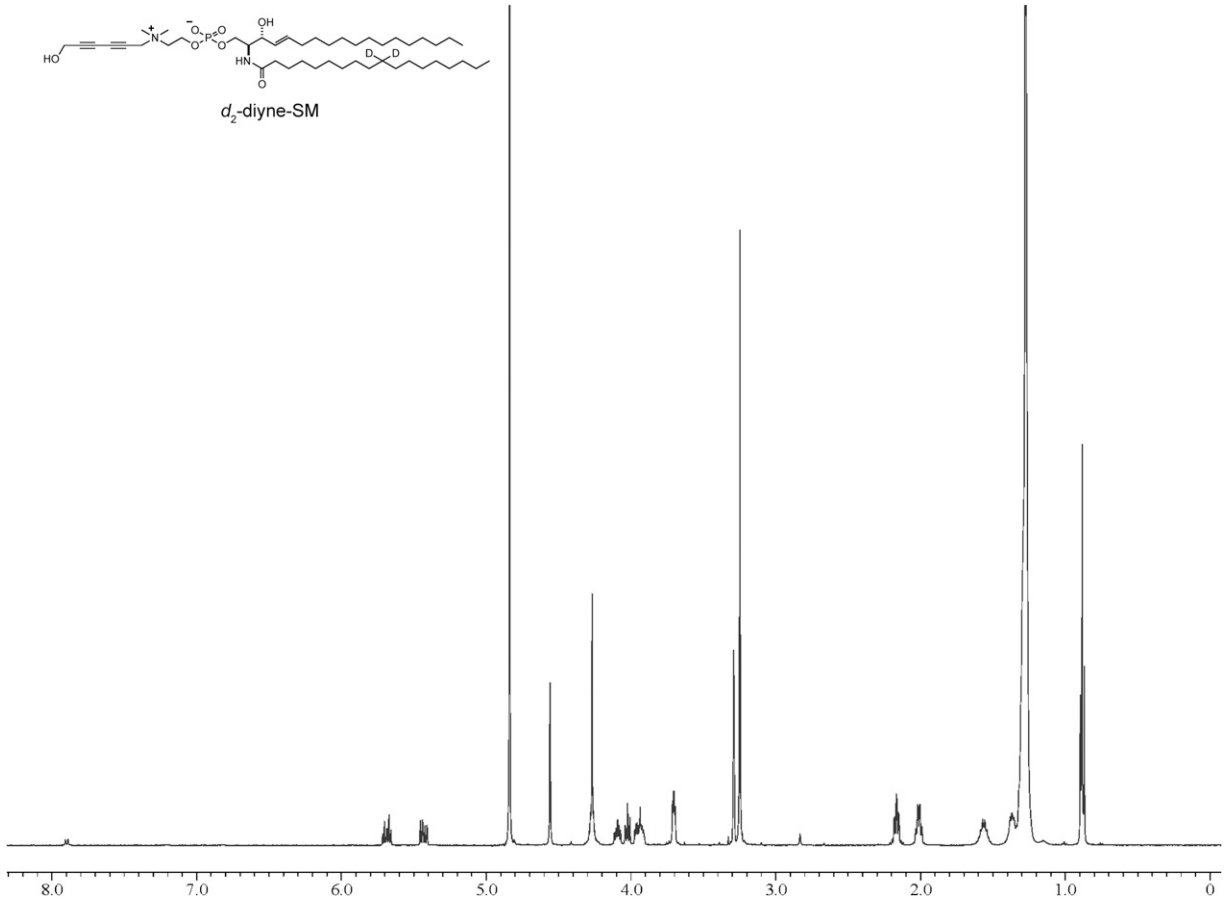

Fig. S11. ^{1}H NMR spectrum of d_2-diyne-SM.

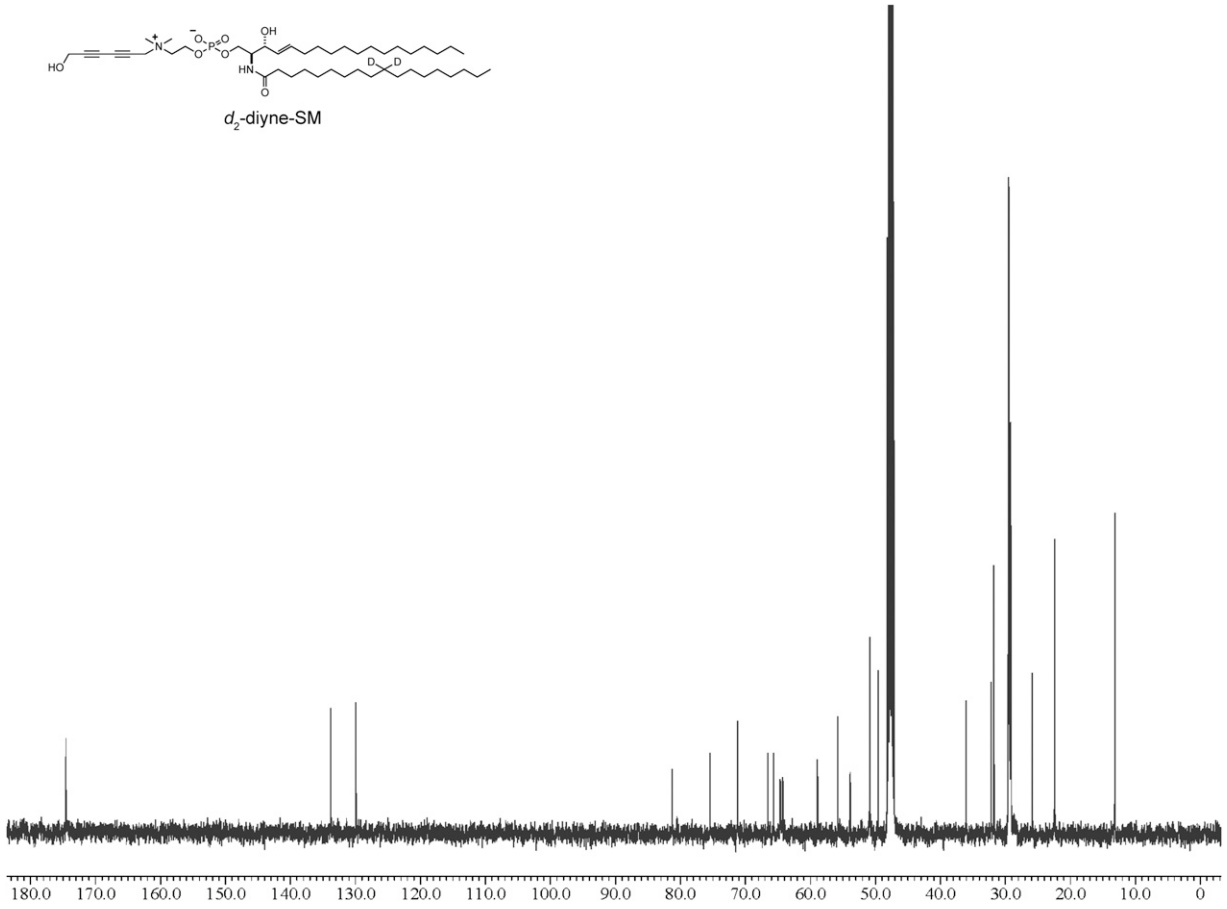

Fig. S12. ^{13}C NMR spectrum of d_2-diyne-SM.

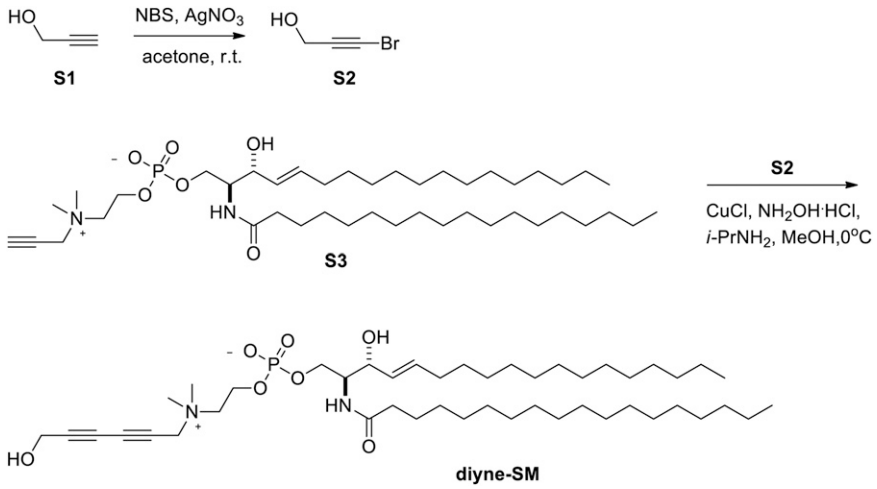

Scheme S1. Synthesis of diyne-SM.

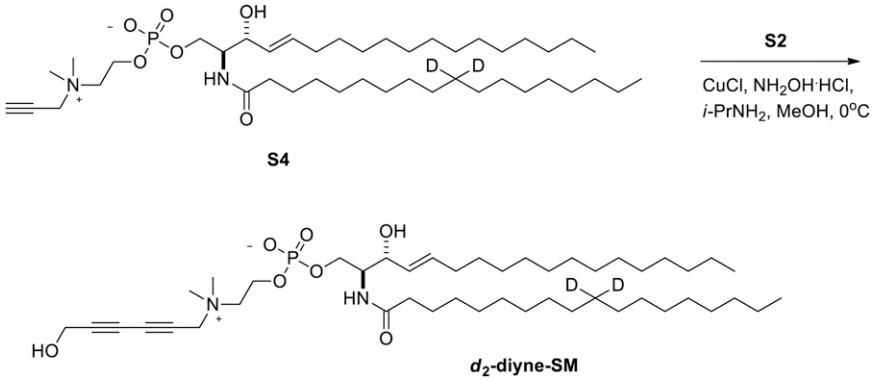

Scheme S2. Synthesis of d_2-diyne-SM.

Table S1. Mean value of Raman intensity of the diyne peak in diyne-SM/DOPC/chol ternary monolayer calculated from the images shown in Fig. S2

Diyne-SM/DOPC/chol	Pixel no.	Mean (± SD)	Relative, %
1:1:1 (ordered)	406	8.01 (± 1.60)	52.2
1:1:1 (disordered)	458	3.54 (± 1.23)	23.1
3:7:3	864	5.29 (± 1.60)	34.5
1:0:0	864	15.35 (± 1.48)	100

Relative value was calculated using diyne peak intensity of the membrane with a 1:0:0 ratio as 100%.